

Research Article

The Self-Healing Capability of Carbon Fibre Composite Structures Subjected to Hypervelocity Impacts Simulating Orbital Space Debris

B. Aïssa,¹ K. Tagziria,¹ E. Haddad,¹ W. Jamroz,¹ J. Loiseau,² A. Higgins,² M. Asgar-Khan,³ S. V. Hoa,³ P. G. Merle,⁴ D. Therriault,^{5,6} and F. Rosei⁷

¹ Department of Smart Materials and Sensors for Space Missions, MPB Technologies Inc., 151 Hymus Boulevard, Pointe-Claire, Montreal, QC, Canada H9R 1E9

² Shock Waves Physics Group and Department of Mechanical Engineering, McGill University, Montreal, QC, Canada H3A 0G4

³ Concordia Center for Composites, Department of Mechanical and Industrial Engineering, Concordia University, Montreal, QC, Canada H3G 2M8

⁴ Center for Applied Research on Polymers (CREPEC), Mechanical Engineering Department, École Polytechnique de Montréal, P.O. Box 6079, Station "Centre-Ville", Montreal, QC, Canada H3C 3A7

⁵ Department of Chemistry and Biochemistry, Concordia University, Canada H3G 2M8

⁶ The Quality Engineering Test Establishment, Department of National Defence, Ottawa, ON, Canada K1A 0K2

⁷ Institut National de la Recherche Scientifique, INRS-Énergie, Matériaux et Télécommunications, 1650 Blvd, Lionel Boulet, CP, Varennes, QC, Canada J3X 1S2

Correspondence should be addressed to B. Aïssa, brahim.aissa@mpbc.ca and E. Haddad, haddad.emile@ymail.com

Received 5 September 2012; Accepted 24 September 2012

Academic Editors: B. Panchapakesan and K. Y. Rhee

Copyright © 2012 B. Aïssa et al. This is an open access article distributed under the Creative Commons Attribution License, which permits unrestricted use, distribution, and reproduction in any medium, provided the original work is properly cited.

The presence in the space of micrometeoroids and orbital debris, particularly in the lower earth orbit, presents a continuous hazard to orbiting satellites, spacecrafts, and the international space station. Space debris includes all nonfunctional, man-made objects and fragments. As the population of debris continues to grow, the probability of collisions that could lead to potential damage will consequently increase. This work addresses a short review of the space debris "challenge" and reports on our recent results obtained on the application of self-healing composite materials on impacted composite structures used in space. Self healing materials were blends of microcapsules containing mainly various combinations of a 5-ethylidene-2-norbornene (5E2N) and dicyclopentadiene (DCPD) monomers, reacted with ruthenium Grubbs' catalyst. The self healing materials were then mixed with a resin epoxy and single-walled carbon nanotubes (SWNTs) using vacuum centrifuging technique. The obtained nanocomposites were infused into the layers of woven carbon fibers reinforced polymer (CFRP). The CFRP specimens were then subjected to hypervelocity impact conditions—prevailing in the space environment—using a home-made implosion-driven hypervelocity launcher. The different self-healing capabilities were determined and the SWNT contribution was discussed with respect to the experimental parameters.

1. Introduction

A major challenge for space missions is that all materials degrade over time and are subject to wear, especially under extreme environments and external solicitations. Impact events are inevitable during the lifetime of a space composite structure, and once they are damaged they are hardly repairable. More specifically, polymeric composites are susceptible to cracks that may either form on the surface or deep within

the material where inspection/detection is often impossible. Materials failure normally starts at the nanoscale level and is then amplified to the micro-up to the macroscale until catastrophic failure occurs. The ideal solution would be to block and eliminate damage as it occurs at the nano/microscale and restore the original material properties.

Self-healing materials are conceived as having the potential to heal and restore their mechanical properties when damaged, thus enhancing the lifetime of materials and

structures. Typical examples of self-healing materials can be found in polymers, metals, ceramics, and their composites which are subjected to a wide variety of healing principles. Healing can be initiated by means of an external source of energy as was shown in the case of a bullet penetration [1] where the ballistic impact caused the local heating of the material allowing the self healing of ionomers, or in the case of self-healing paints used in the automotive industry. In the latter case, small scratches can be restored by solar heating [2]. Single cracks formed in poly(methyl methacrylate) (PMMA) specimens at room temperature were also shown to be completely restored above the glass transition temperature [3]. The presence of noncovalent hydrogen bonds [4] in mechanosensitive polymers can allow a rearrangement of principal chemical bonds so that they can be used for self-healing. However, noncovalent processes may limit the long-term stability in structural materials. Force induced covalent bonds can be activated by incorporating mechanophores (mechanically sensitive chemical groups) in polymer strands [5]. Numerical studies have also shown that nanoscopic gel particles, which are interconnected in a macroscopic network by means of stable and labile bonds, have the potential to be used in self-healing applications. Upon mechanical loadings, the labile bonds break and bond again with other active groups [6]. Contact methods have also been investigated where the self-healing of the damaged samples is activated with a sintering process which increases the contact adhesion between particles [7]. Although these approaches are quite interesting, it is believed that the most promising methods for self-healing applications involve the use of nano/microparticles [8], hollow tubes and fibres [9], microcapsules [10], nanocontainers [11], or microfluidic vascular systems [12], filled with a fluid healing agent (e.g., epoxy for composite materials [13], corrosion inhibitor for coatings [14], etc.) and dispersed in the hosting material. When the surrounding environment undergoes changes such as temperature, pH, cracks, or impacts, then the healing agent is released. These techniques are, however, limited by the container size. Containers should be in the micro/nanoscale range since larger containers could lead to large hollow cavities which could compromise the mechanical properties of the hosting structural material or the passive protective properties of the coating material [8].

On the other hand, with their well-known excellent mechanical and electrical properties, carbon nanotubes (CNTs) are inherently multifunctional and can serve as an ideal structural reinforcement. Considerable interest has focused on using CNTs as a passive reinforcement to tailor their mechanical properties [15]. This is due to the fact that CNTs are very small; thus they have an extremely large interfacial area, have very interesting mechanical and chemical properties, and have a hollow tubular structure. In fact, various materials such as hydrogen (H_2), metal/metal carbide, and DNA [16–19] have been inserted inside these nanometer-sized tube-like structures. Although a great deal of work has been done with CNT-networks for the in situ sensing of impact damage in composite materials (thanks to their electrical properties) [20], CNTs have not been

yet investigated properly and largely as reinforcement for self-healing applications.

In this work, we successfully developed self healing materials composites, consisting of different blends of microcapsules containing various combinations of a 5-ethylidene-2-norbornene (5E2N) and dicyclopentadiene (DCPD) monomers, reacted with the ruthenium Grubbs' catalyst. The self healing materials were then successfully mixed with an Epon 828 based resin epoxy and single-walled carbon nanotubes (SWNTs) materials and infused into the layers of woven carbon, fibers reinforced polymer (CFRP). The CFRP specimens structures were then subjected to hypervelocity impact conditions—prevailing in the space environment—using a home-made implosion-driven—hypervelocity launcher. Finally, the impacted CFRP specimens were systematically characterized with the three-point bending tests for flexural strengths evaluation, where both the self-healing efficiency and the CNT contribution were discussed.

2. Review

2.1. Fibre Bragg Grating Sensor. The optic fibres are cylindrical silica waveguides. They consist of a core surrounded by a concentric cladding, with different refraction index, guaranteeing the light propagation (Figure 1(a)). Fibre Bragg gratings (Figure 1(b)) are formed when a periodic variation of the index of the refraction of the core is created along a section of an optic fibre, by exposing the optic fibre to an interference pattern of intense ultraviolet light [21]. The photosensitivity of silica glass permits the index of refraction in the core to be increased by the intense laser radiation λ_B .

If broadband light is travelling through an optical fibre containing such a periodic structure, its diffractive properties promote that only a very narrow wavelength band is reflected back (Figure 2). The centre wavelength, λ_B , of this band can be represented by the well-known Bragg condition:

$$\lambda_B = 2\mathbf{n}_0 \cdot \Lambda_B, \quad (1)$$

where Λ_B is the spacing between grating periods and \mathbf{n}_0 is the effective index of the core. Fibre Bragg grating sensors are wavelength-modulated sensors. Gratings are simple, intrinsic sensing elements and give an absolute measurement of the physical perturbation they sense. Their basic principle of operation is to monitor the wavelength shift associated with the Bragg resonance condition. The wavelength shift is independent of the light source intensity. Their characteristics justify that they are the favourite candidate for strain and temperature sensing.

At constant temperature for a longitudinal strain variation, $\Delta\epsilon$, the corresponding wavelength shift is given by

$$\begin{aligned} \Delta\lambda_B &= \lambda_B \left(\frac{1}{\Lambda_B} \cdot \frac{\partial\Lambda_B}{\partial\epsilon} + \frac{1}{\mathbf{n}_0} \cdot \frac{\partial\mathbf{n}_0}{\partial\epsilon} \right) \Delta\epsilon \\ &= \lambda_B (1 - \mathbf{p}_e) \Delta\epsilon, \end{aligned} \quad (2)$$

where \mathbf{p}_e is the effective photo-elastic coefficient of the optical fibre. For a silica fibre, the FBG wavelength-strain sensitivity at 1550 nm, for example, is of $1.15 \text{ pm } \mu\epsilon^{-1}$ [22].

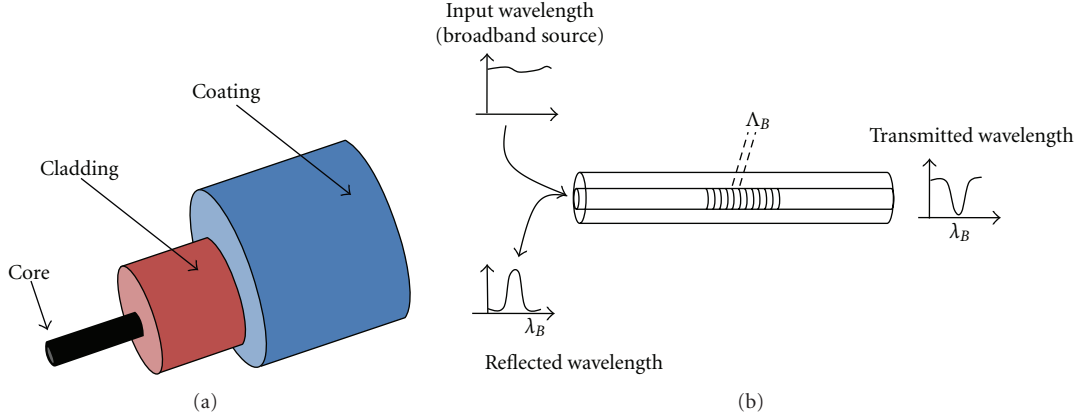


FIGURE 1: (a) Description of the optical fibre. (b) Fibre Bragg grating concept.

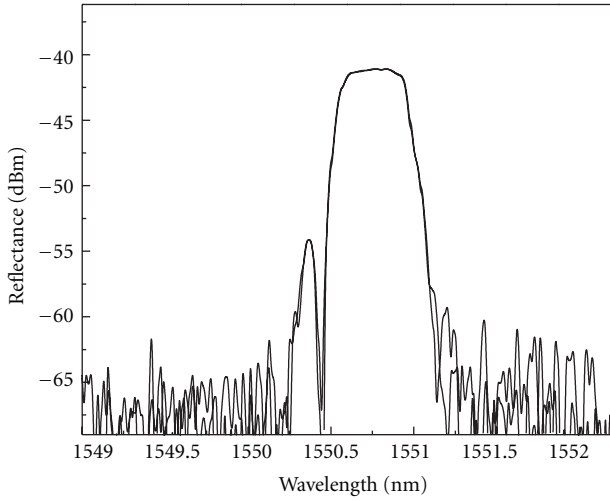


FIGURE 2: Typical optical power spectrum (reflectance in dBm) of our embedded FBG.

In our present work, we used an ultrafast 2 MHz FBG interrogator to view the Bragg wavelength shifts equipped with an integrated computer with the appropriate data acquisition software for flexibility in data display, processing, and storage of all information observed. Figure 2 shows a representation of the optical power spectrum of one of our fabricated FBG observed at the optical spectrum analyser.

When an axial stress is applied to the optical fiber, the reflected spectrum wavelength shifts. This shift is to make wavelengths for axial tension higher and to lower wavelengths for axial compression. The axial strain applied to the optical fiber at the location of FBG can be calculated from the shift in the peak wavelength as follows:

$$\epsilon = \frac{\Delta\lambda}{\lambda_B}(1 - p_e), \quad (3)$$

where $\Delta\lambda$ is the peak wavelength shift (reported as centre wavelength (CWL) in the present work), λ_B is the original Bragg wavelength, p_e is the effective strain-optic coefficient for the optical fiber fundamental mode, and ϵ is the axial strain [23]. When nonuniform axial strains or transverse

stress components are applied to the optical fiber, the reflected spectrum of the FBG is no longer a simple reflected peak. The reflected spectrum can broaden or take the form of multiple peaks or a more complex spectral form as shown in the schematic of Figure 3. This spectral distortion is often used to detect the presence of stress. For nonhydrostatic loading cases, the transverse loading creates birefringence in the optical fiber, leading to two axes of propagation in the fiber. The light wave propagating through the fiber is split into two modes, each experiencing a slightly different Bragg wavelength, as they pass through the FBG. When recombined, the reflected spectrum demonstrates two distinctive peaks as shown in the schematic of Figure 3. The wavelength separation between these peaks is proportional to the magnitude of the transverse stress component [24]. Additionally, nonuniform axial strain along the FBG can further distort the response spectrum as also shown in Figure 3.

2.2. Review of Effects of Space Debris on Space Materials

2.2.1. Small Debris and Micrometeorites.

Space debris coming from human devices set in space mainly occurs in Low Earth Orbital (LEO) below 2000 km and around the geostationary orbit (GEO) altitude. Meteoroids, which are natural phenomena, are found everywhere in space. However,

- (i) impact effects from meteoroids and debris are similar,
- (ii) average impact velocities in LEO are 10 km/s for space debris and 20 km/s for meteoroids:

$$\begin{aligned} \text{orbital debris : } V_{\text{impact}} &= 2\text{--}15 \text{ km/s,} \\ \text{natural micrometeoroids : } V_{\text{impact}} &= 2\text{--}72 \text{ km/s,} \end{aligned} \quad (4)$$

- (iii) average material density of meteoroids is lower than that of the space debris,
- (iv) in LEO, meteoroids dominate for sizes between 5 and 500 microns (0.5 mm),
- (v) space debris dominates for larger sizes.

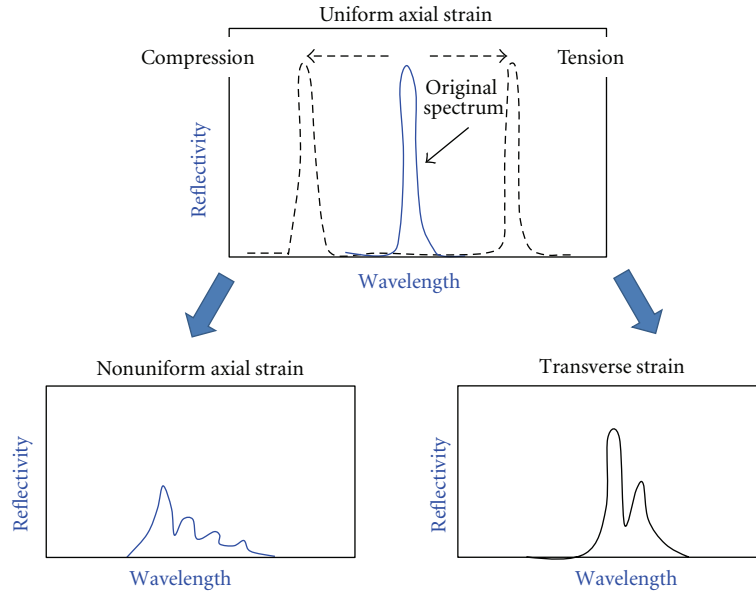


FIGURE 3: Schematic of FBG sensor reflected spectrum under various strain states.

Micrometeoroids are small particles from an asteroid or comet orbiting the sun (called meteoroids) that survives their passage through the Earth's atmosphere and impacts the Earth or the satellite surface [25].

Hypervelocity impact events may modify the original chemical composition of an impactor, fractionating volatile from refractory elements. Thus micrometeoroid residues may not necessarily retain the stoichiometric chemical signature of their parent mineral; in this case analytical results are not easily compared to those of mineral standards. Notwithstanding such difficulties, Energy Dispersive (EDS) spectra and X-ray elemental maps of residues that contain the following elements can be used as indicators of a micrometeoroid origin [25]:

- (i) Mg + Si + Fe (mafic silicates, e.g., olivine or orthopyroxene),
- (ii) Mg, Ca, Na, Fe, Al, Ti + Si (clinopyroxene),
- (iii) Fe + S (Fe-sulfides),
- (iv) Fe + Ni (minor or trace) + S (Fe-Ni sulfides),
- (v) Fe + Ni concentration at meteoritic levels (metal),
- (vi) Si + C (silicon carbide),
- (vii) Fe, Mg, Al + Si (phyllosilicates, e.g., serpentine),
- (viii) Ca, C, O (calcite),
- (ix) K, Cl, P, and Cr have also been individually identified in meteoritic samples; therefore, may be indicative of a micrometeoroid origin under some circumstances.

Because of the complexity of any original micrometeoroid (polymineralic composition), it is possible that a single impactor could be any one of many combinations from the above list.

2.2.2. *Space Debris.* The remnants of space debris material may be identified from the residue chemistry of the EDS spectra and X-ray elemental maps that contain the following elements [25]:

- (i) mainly Ti + possible minor C, N, O, and Zn (paint fragment),
- (ii) mainly Fe + variable Cr, Mn + possible trace Ni (specialised steels),
- (iii) mainly Al + minor Cl, O, and C (rocket propellant),
- (iv) mainly Sn + Cu (computer or electronic components),
- (v) enrichments in Mg, Si, Ce, Ca, K, Al, and Zn (glass impactor, possibly from other solar cells).

The presence of the Ti/Al layer within the solar cell complicates the identification of artificial impacts since Ti has been traditionally used as an indicator of paint fragment impact. In the Hubble Space Telescope, solar cells containing Ti, Al, and Ag, were ascribed to artificial debris particles, such as paint fragments. Thus, whilst Ti on its own state is probably a good indicator of paint fragments, when observed along with Al and Ag, it is more likely to represent a melt from the host solar cell.

The classification of impact residues in terms of either space debris or micrometeoroid in origin is extremely complex, and often it is not possible to give a totally unambiguous answer. For example, although it is highly likely that a residue composed of Al and O is the remnant of solid rocket motor debris (Al_2O_3), it could conceivably also be corundum (Al_2O_3) which has been identified in primitive meteorites, although it is extremely rare.

2.2.3. *Contamination.* Apart from the classification criteria given for the residual material of either micrometeoroid or

TABLE 1: Summary of a number of objects orbiting in space.

Category (and origin)	Size	Numbers in orbit	Probability of Collision (and effects)
Large debris (Satellites, rocket bodies, fragmentation material).	>10 cm	$1-5 \times 10^4$ (Low) (17,800 in 2001)	1/1000 (collision results in total breakup and loss of capability)
Medium Fragmentation debris, explosion debris, leaking coolant.	1 mm–10 cm	$1-5 \times 10^6$ (Medium) (0.5×10^6 in 2001)	1/100 (collision could cause significant damage and possible failure)
Small Aluminum oxide particles, paint chips, exhaust products, bolts, caps, meteoric dust.	<1 mm	$>10^{12}$ (High) (3×10^8 in 2001)	Almost 1/1 collision should cause insignificant damage

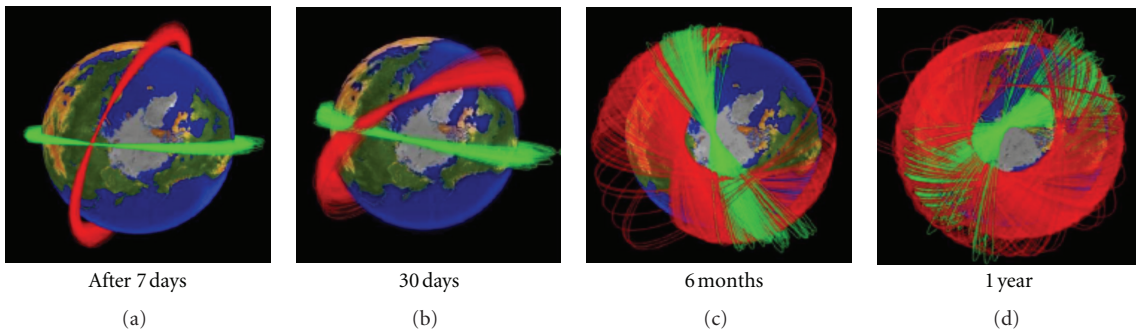


FIGURE 4: Spread of collision debris orbital planes. Adapted from [26].

space debris origin, there is a strong possibility that spacecraft and satellites surfaces may also be subject to contamination. There are several different possible sources of contamination, arising from laboratory handling, to ground exposure, to space environment itself whereby contaminants are effectively encountered at low velocity and are thus only loosely bound.

2.2.4. Main Effects of Space Debris Micrometeorites. Hypervelocity impacts create a shock wave in the material and lead to very high pressures (>100 GPa) and temperatures superior to 10000°K. Further detailed supplementary information is given, for example, in the *ESA space debris mitigation handbook* of [27]. However,

- (i) the impact process lasts only a few microseconds,
- (ii) the impactor and target material are fragmented, often molten and/or vaporised, depending on the impact velocity and materials,
- (iii) most of the impact energy ends up in the *ejecta* (i.e., ejected mass),
- (iv) the ejected mass can be much larger than the mass of the impactor,
- (v) a small fraction (less than 1%) of the ejected material is ionized; this latter phenomenon is function of the impactor velocity.

On the other hand, collision damage (Table 1) depends on:

- (i) kinetic energy of the particle (speed),
- (ii) design of the spacecraft (bumpers, external exposure points),
- (iii) collision geometry (especially the angle of collision),

The impact ranges are of about:

- (i) 1 cm (medium) at 10 km/sec: this can fatally damage a spacecraft,
- (ii) 1 mm and less: which erode thermal surfaces, damage optics, and puncture fuel lines.

The near space environment is actually very polluted by significant traces of recent human space history. All the space vehicles that have left the earth participated to this evolution of collision risks in space for active spacecraft. The population of space debris is composed of a very large variety of parts from the smallest (less than a millimetre) up to complete vehicles (up to several tons for lost spacecraft) through all debris issued from vehicles (rocket stages for example) explosions (Figure 4).

The use of CFRP in space structures has largely spread, it can be noticed through the number of papers dedicated to study its reliability, health monitoring in space, its response to debris.

Typical satellite service modules are square or octagonal boxes with a central cone/cylinder and shear panels. The cone

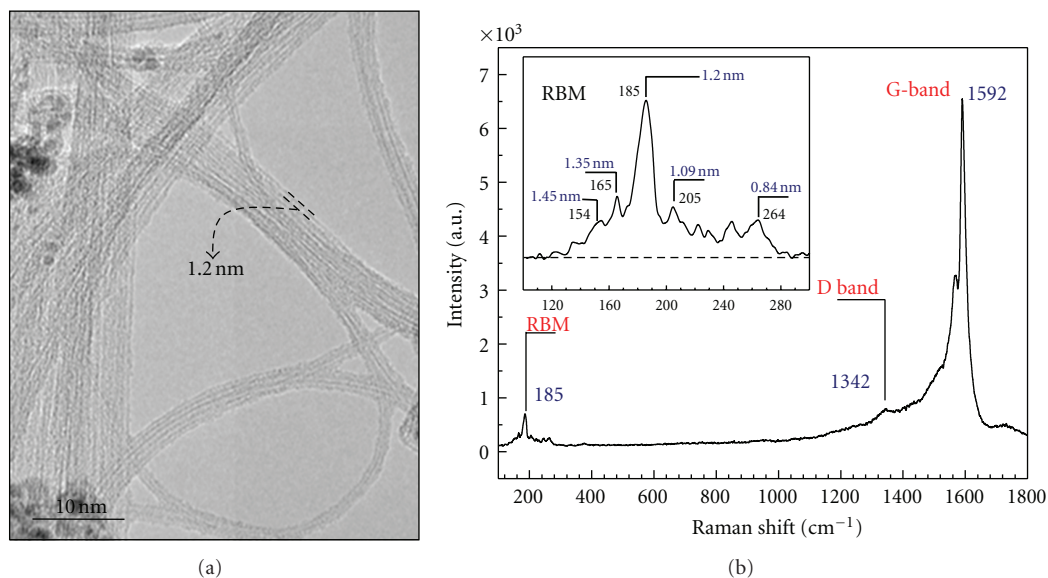


FIGURE 5: Morphology of the grown SWCNTs: (a) representative TEM images of the SWNT materials. The inset is aHRTEM closeup showing nanotubes of 1.2 nm-diam. (b) Typical Raman spectrum of the nanotube materials, where the various RBM, D, and G bands are clearly identified. The inset shows a close-up of the RBM band located at 185 cm^{-1} , corresponding to an individual SWCNT having a mean diameter of 1.2 nm in total agreement with the TEM analysis in (a).

cylinder and shear panels (SP) are generally constructed from a sandwich panel with CFRP face sheets and an aluminium honeycomb (HC) core (CFRP/Al HC SP). Similarly, the upper and lower platforms are also CFRP/Al HC SPs. The lateral panels of the service module are, due to thermal reasons, generally sandwich panels with aluminium face sheets and aluminium honeycomb cores. These panels are also generally wrapped with multilayer insulation blankets (MLIBs).

Lateral panels may be made with CFRP/Al HC SP. Other payloads include telescopes, which require a specific design quite often constructed predominantly of CFRP (for stability and pointing requirements). Truss-type structures are often used for supporting antennas, solar arrays, and so forth, typically made of CFRP.

3. Experimental Setup

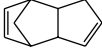
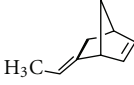
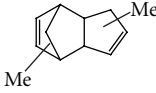
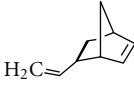
3.1. CNT Growth and Characterization. Single-walled carbon nanotubes (SWCNTs) materials have been synthesized by using the developed plasma torch technology (detailed process can be found in [28, 29]). In this approach, a carbon containing ethylene (C_2H_4) substance combined with gaseous catalyst based ferrocene ($\text{Fe}(\text{C}_5\text{H}_5)_2$) vapour are injected in an inert gas plasma jet. The inert gas is a mixture of 50% argon with 50% helium. The hot temperature of the plasma ($\sim 5000\text{ K}$) is capable to dissociate the ethylene and ferrocene molecules to produce iron and carbon vapour. These atomic and molecular species are rapidly cooled to a rate of 10^5 K/s in a warmer environment of about 1273 K . The process exclusively produces SWCNT materials, and the growth takes place in the gas phase. The as-grown soot-like SWCNTs were purified by an acidic treatment through refluxing in a 3 M-HNO_3 solution for 5 h at 130°C , and

subsequently filtered. The plasma-grown carbon nanotubes were characterized by scanning electron microscopy (SEM). Bright field transmission electron microscopy (TEM) was also performed. The Raman measurements were performed with the 514.5 nm (2.41 eV) laser radiation of an Ar^+ laser focused onto the sample with a spot of $1\ \mu\text{m}$. The Raman spectra were taken with a backscattering geometry at room temperature in the $100\text{--}2000\text{ cm}^{-1}$ spectral region. Figure 5(a) shows representative TEM micrographs of the purified SWCNT deposit, where bundles of a few single-walled nanotubes (the diameter of the single tubes is about 1.2 nm) are clearly seen. A typical Raman spectrum (Figure 5(b)) of the SWNT materials shows clear scattering peaks appearing in the low ($100\text{--}300\text{ cm}^{-1}$) and high ($\sim 1600\text{ cm}^{-1}$) frequency regions, corresponding to the radial breathing mode (RBM) and the tangential vibrating mode (G), respectively, which are the fingerprints of the presence of SWNTs. The RBM peak centered at 185 cm^{-1} is attributed to the strong presence of single-walled carbon nanotubes having a mean diameter of 1.2 nm according to the formula of Bandow et al. [30] (in total agreement with the TEM observations). The D-peak centered around 1350 cm^{-1} is due to the presence of amorphous and/or disordered carbon structures. Nevertheless, the rather very low D-to-G peak intensity ratio (~ 0.05) is worth noting, which indicates the overall high quality of the SWCNTs mats.

3.2. Selection of the 5E2N Monomer. All the chemicals (Grubbs, catalyst first generation, monomers, etc.) were used as received.

Due to the relatively high freezing temperature of dicyclopentadiene (DCPD), another monomer with larger functional temperature range was necessary. A number of candidates were evaluated, as shown in Table 2. Among

TABLE 2: Comparison between different monomers [31].

Compound	Toxicity	T_{melt} ($^{\circ}\text{C}$)	T_{boil} ($^{\circ}\text{C}$)	CAD\$/L
Dicyclopentadiene (DCPD)	Flammable, harmful 	32.5	170	~70
5-Ethylidene-2-norbornene (5E2N)	Harmful 	-80	148	~85
1,5-Cyclooctadiene (COD)	Harmful 	-69	150	~75
Methylcyclopentadiene dimer (MCPD)	Poisonous 	-51	70–80	~60
5-Vinyl-2-norbornene (5V2N)	Harmful 	-80	141	~160

these candidates, the monomer 5-ethylidene-2-norbornene (5E2N) is a liquid from -80 to 148°C , with faster ROMP reaction that is DCPD [32, 33]. Also, from the cost and toxicity point of view, this monomer is more attractive than the others.

While 5E2N has a wider liquid temperature range than DCPD, it is important to investigate its stability. The self healing technique was tested in vacuum and over a long time. To permit simple curing, the selected monomers for the self-healing have to comply with the following requirements: (i) must be air stable, (ii) undergo a romp opening metathesis polymerisation (ROMP) reaction.

The study permitted a preliminary selection of the following compounds summarized in Table 2:

- (i) dicyclopentadiene, DCPD,
- (ii) di(methylcyclopentadiene), DMCP,
- (iii) 5-ethylidene-2-norbornene, 5E2N,
- (iv) 5-vinyl-2-norbornene, 5V2N,
- (v) 1,5-cyclooctadiene, COD.

Hence, as mentioned above, the 5E2N was selected as the optimal monomer with very wide range of temperature functionality [-80 to $+148^{\circ}\text{C}$] and is less expensive and better relative to safety and environment (toxicity and flammability).

4. The 5E2N Monomer Encapsulation

For the fabrication stage, the first issue is to achieve a controlled microencapsulation synthesized with desired characteristics (e.g., size, shell thickness, healing content, etc.) and desired properties (e.g., microcapsules having a rough

surface morphology that aids in the adhesion of the microcapsules with the polymer matrix during composite processing). One should note here that all the involved materials must be carefully engineered. For example, the encapsulation procedure must be chemically compatible with the reactive healing agent, and the liquid healing agent must not diffuse out of the capsule shell during its potentially long shelflife. At the same time, the microcapsule walls must be enough resistant to processing conditions of the host composite, while maintaining excellent adhesion with the cured polymer matrix to ensure that the capsules rupture upon a composite fracture. The second issue is hence to disperse the microcapsules as well as the catalysts, appropriately into the matrix materials (Epon 828 with Epicure 3046), and finally making the sample. The samples are then tested by creating certain damages into it, and healing performance is observed.

The encapsulation of the 5-ethylidene-2-norbornene 5E2N in poly(melamine-urea-formaldehyde) microcapsules was achieved following the protocol here below. The drying of the microcapsules was improved by rinsing them successively with deionised water and acetone.

Microcapsules are synthesized according to the flowchart in Figure 6. The process is inspired from the one described in [31]. Several batches of microcapsules were produced following the reported process. The size of the microcapsules was mainly controlled by varying the stirring speed during the synthesis process. Some samples of the smallest microcapsules synthesized from different batches are shown in Figure 7. All samples were dried in air for at least 24 hours after their final washing and filtering. Separating the microcapsules from the dross is found to be the main challenge of the process. Figure 7(a) shows typical optical micrographs of microcapsules produced with stirring speed of 1200 rpm. It can be seen from the above SEM images that the average size of the microcapsule produced is sometimes around 5

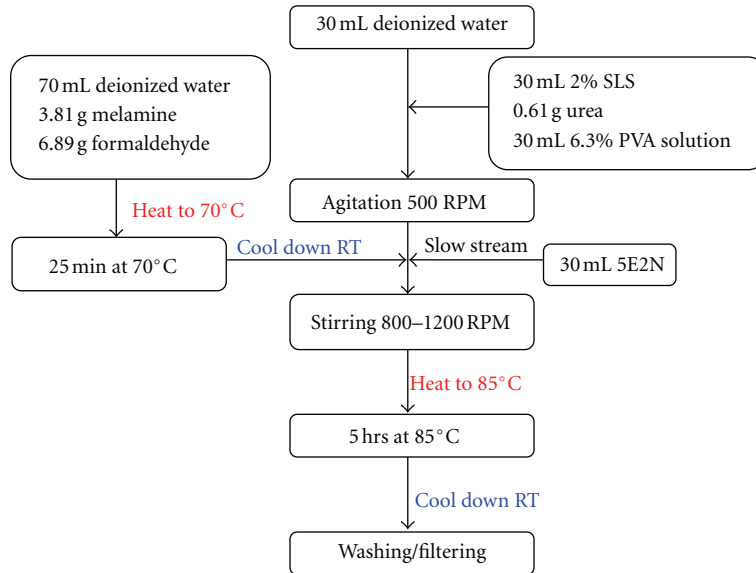


FIGURE 6: Flowchart for preparing 5E2N/poly(melamine-urea-formaldehyde) (PMUF) microcapsules.

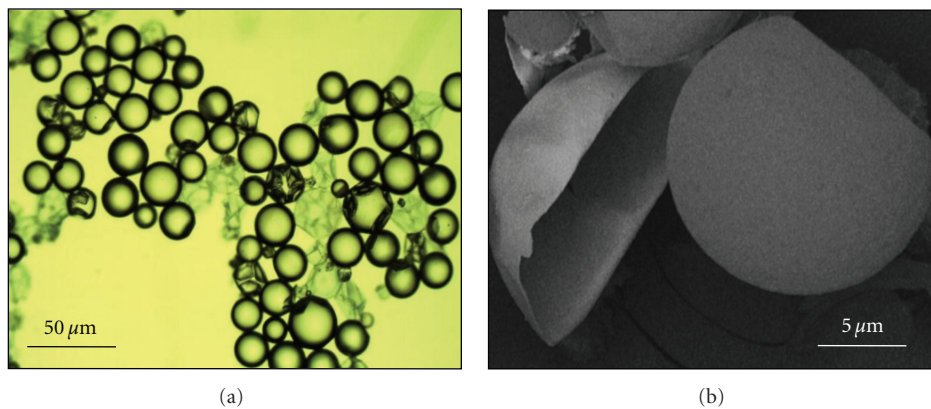


FIGURE 7: 5E2N monomer encapsulation (a) typical optical photo, followed by (b) scanning electron microscope (SEM) image of the small microcapsule showing the core-shell structure of the encapsulation.

microns. However, a few microcapsule shells are found to break, which is possibly due to the high current/voltage used during the preparation of SEM specimen.

The detailed process of the 5E2N encapsulation and the effect of the whole involved synthesis parameters on the capsule size and their corresponding healing efficiency will be the subject of a separate publication.

4.1. Chemical Constituents. The self-healing demonstrator consisted of woven CFRP samples, containing three main constituents.

- (i) Host matrix: an epoxy prepolymer (Epon 828) and a curing agent (Epicure 3046); this epoxy is used in space for internal structures
- (ii) Microcapsules: the monomer healing agents (5E2N) prepared as small microcapsules (diameter less than 15 microns); the monomer is homogeneously spread

within the epoxy and forms about 10% of the structure weight.

- (iii) Different concentrations of single-walled carbon nanotubes materials.
- (iv) Catalyst: Grubbs catalyst first generation (ruthenium metal catalyst); In order to polymerize, the healing agent must come into contact with a catalyst. A patented catalyst, called Grubbs' catalyst, is used for this self-healing material. It is important that the catalyst and healing agent remain separated until they are needed to seal a crack.
- (v) The healing chemical process that permits the reaction between the monomer and the catalyst is called ROMP—Ring Opening Metathesis Polymerization.

4.2. Monomer Diffusion under Vacuum. The diffusion of the monomer from the pure microcapsules in vacuum was

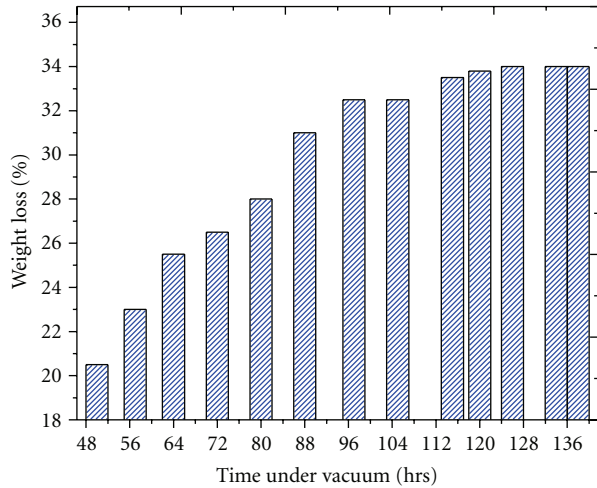


FIGURE 8: Microcapsules % weight loss under vacuum as a function of time.

measured by placing a weighted amount of capsules in a Schlenk tube under vacuum (10^{-2} mbar) for an extended period of time. We see from Figure 8 that the histogram presents a plateau in the weight loss is reached after 5 days (34% in weight; i.e., about 50% of the initial monomer content of the microcapsule is lost). The monomer loss seems to proceed by steps.

5. Fabrication of Woven CFRP Samples Embedded Microcapsules Containing 5E2N and DCPD Monomers and Grubb's Catalyst

The CFRP samples containing self-healing demonstrator consists of epoxy used in space for internal structures (Epon 828 resin, with the Epicure 3046 curing agent) and 2 different healing agents (namely, 5E2N, DCPD) prepared as small microcapsules (diameter less than 15 microns) kept within thin shells of polymelamine (urea-formaldehyde). The monomer is homogeneously spread within the epoxy, and forms about 10% of the total weight. The Grubbs catalyst was then distributed within the epoxy structure (1 to 2% of the total weight). Different series of samples specimens were prepared, with and without CNTs.

After the hypervelocity impact tests, the crack formed on the CFRP samples reaches a microcapsule and causes its wall rupture, which releases the healing agent monomer (5E2N or DCPD or the combination of the two monomers as will be detailed below) in the crack. Once the monomer and catalyst enter in contact, the self-healing reaction is triggered (i.e., polymerization between the healing agent (monomer) and matrix-embedded catalyst particles) [31, 34–43]. The Grubbs, catalyst will sustain the chemical reaction known as Ring Opening Metathesis Polymerization (ROMP), up to the time the crack and the open microcapsule are full.

The use of the 5E2N monomer can be considered as an innovative healing method, since none of the chemical products proposed previously would be functional, in space

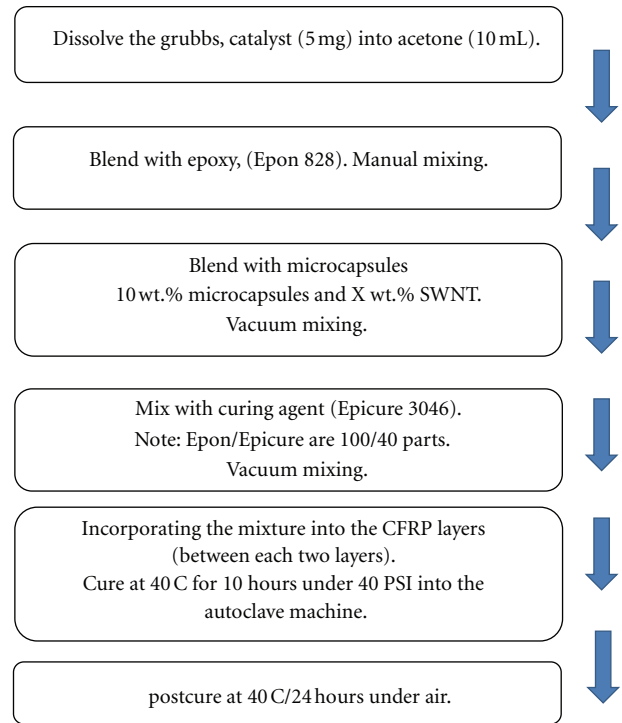


FIGURE 9: Fabrication procedure of the manufacturing of CFRP with self healing and FBG sensors.

environment conditions, because the DCPD monomer melting temperature is 33°C (i.e., it is in the solid phase at room temperature), and the chemical activities are somehow relatively slow, with the risk of evaporation during the reaction. However, the drawback to using this monomer is that the resulting polymer is linear and thus it has inferior mechanical properties as compared to DCPD. We propose a route towards the combination of these two monomers thereby obtaining simultaneously a fast autonomic self-repair composite with excellent mechanical properties. In a second step, we aim at combining the known higher mechanical properties of CNT materials with these monomers to evaluate the self healing capability.

5.1. Manufacturing of CFRP with Self-Healing Materials and FBG Sensors. The fabricated microcapsules containing the healing agent monomer were embedded into a woven carbon fiber reinforced polymer (4 woven layer were used and the average size of the microcapsules is equal or less than $15\ \mu\text{m}$ diam.) The fabrication procedure is summarized in Figure 9. The FBG sensors were embedded between the 2nd and 3rd CFRP layer, but concentrated inside a circle surface of 5 cm-diam (Figure 10), corresponding to the exposed area to debris during the hypervelocity impact experiment.

5.2. Hypervelocity Impact Tests. Impact tests were performed with the implosion-driven hypervelocity launcher using the CFRP composite samples described above. The sample (i.e., CFRP+FBG) was mounted in the target chamber (see schematic of Figure 11(a)), which was flushed with

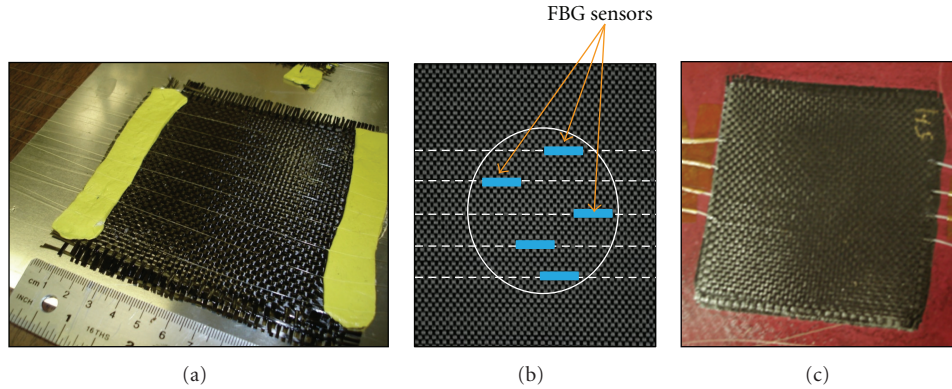


FIGURE 10: (a) Integration of 4–8 FBGs sensors embedded between 2nd and 3rd CFRP layer and concentrated inside a circle surface of 5 cm-diam. corresponding to the exposed area to debris during the hypervelocity impact experiment. (b) Final prototype of the sample.

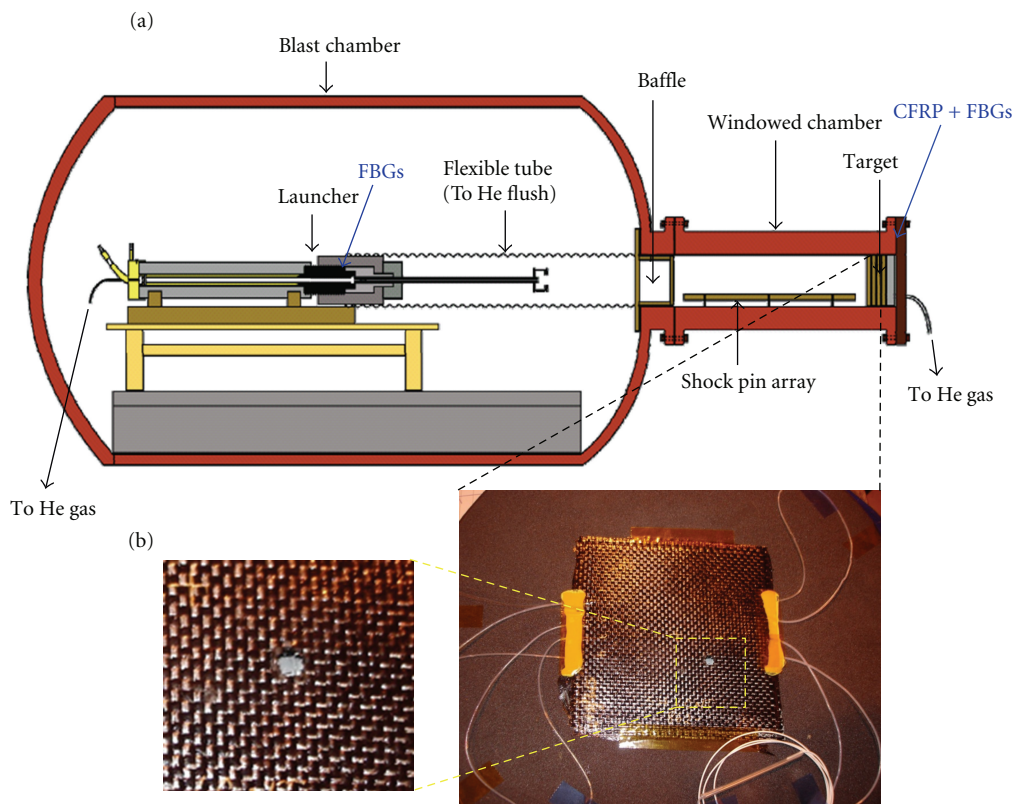


FIGURE 11: (a) Schematic of the launcher and the FBGs. Some FBGs were installed on the explosion tube (launcher), and some at the end of the tube within the CFRP sample. (b) Typical example of the CFRP samples containing FBG sensors after shooting under the hypervelocity impact.

helium gas. The implosion-driven hypervelocity launcher functioned properly and to simulate the orbital space debris, small bore and/or polycarbonate projectiles (3–4 mm-diameters) were launched properly, and velocities ranging from 4 to 8 km/s were employed.

All the fabricated samples are tested under the same conditions for a comparison purpose. The impact resulted in the complete penetration of the sample and a significant amount of delamination on both sides of the sample (Figure 11(b)).

In addition, frequent secondary impacts also occurred, likely a result of fragments generated by the hypervelocity launcher.

Since the impact is supposed to produce delaminations within the CFRP sample, we first attempted to quantify these delaminations through their nominal thickness. This represents the ratio of the thickness after/before impact experiment.

The thicker zone should then correspond to where the delamination occurred. To do so, the CFRP sample is cut into

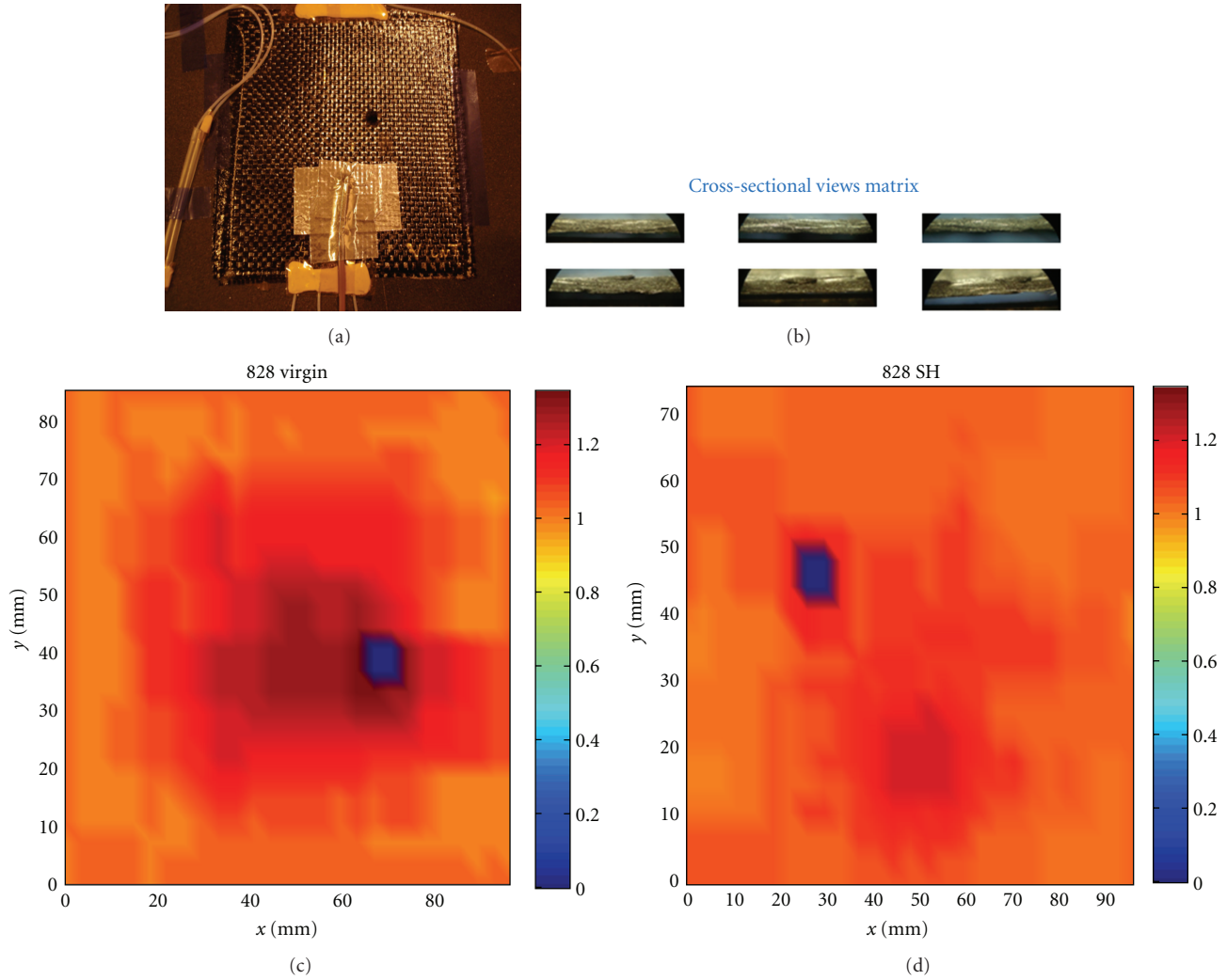


FIGURE 12: (a) Optical photo of the CFRP structure after impact tests, (b) representative cross-sectional view optical photos of the CFRP sample. Color code diagram simulation of the impacted sample in cases (c) with and (d) without self healing materials.

slices, and the matrix thicknesses were built by the estimation of the thickness through the cross-sectional optical photos (thickness is estimated each 3 mm step in the 2 dimensions of the square sample (12 cm × 12 cm), and matrix of more than 650 values is obtained for each case and each sample under study.) We have then used an appropriate software code to trace two dimensions color graphic, where the color indicates the width (/thickness) of the zone (wider zone is where the delamination is larger). Figure 12 shows a typical example of color code diagram obtained for CFRP based Epon 828, in case with and without (i.e., pristine sample) self healing materials (5E2N microcapsules reacted ruthenium Grubbs' catalyst).

Two main conclusions were drawn.

- (i) The color code diagram indicates that the thicker portion of the sample containing delaminations is more localised around the impact zone, especially in the case of the self healing samples.

- (ii) The thickness distribution of the CFRP samples containing self healing material seems to be much more homogenized comparatively to the pristine one (i.e., pure Epon 828), which indicates a clear healing effect (i.e., less delamination propagation after the healing process).

Impacted CFRP samples have been measured under the flexural “3-point bending test” after the healing process (48 hours and 40°C) to investigate their mechanical properties. Each sample was cut into 7 to 8 slices as shown in Figure 14(c).

Flexural tests were performed twice:

- (i) one measurement after the hypervelocity impact and healing process (48 hours, 40°C) and
- (ii) a second measurement after a second healing process (48 hours, 40°C).

The mechanical measurement performed on the slice where the impact crater is located is taken as a reference to

TABLE 3: Summary of the impacted CFRP structures. All the self-healing materials are mixed with 1 wt.% of ruthenium Grubbs, catalyst and 10 wt.% of microcapsules.

	Number of woven CFRP layer	Number of embedded FBG sensors	Embedded material	Mechanical strength (MPa)	Healing efficiency %
Set no. 1	4	4	Virgin Epon 828	245	45
Set no. 2	4	4	Epon 828 + microcapsules 5E2N	276	58
Set no. 3	4	4	Epon 828 + microcapsules DCPD	290	63
Set no. 4	4	4	Epon 828 + microcapsules (5E2N + DCPD)	281	61
Set no. 5	4	4	Epon 828 + microcapsules (5E2N + DCPD) + 0.5 wt.% CNT	297	68
Set no. 6	4	4	Epon 828 + microcapsules (5E2N + DCPD) + 1 wt.% CNT	310	74
Set no. 7	4	4	Epon 828 + microcapsules (5E2N + DCPD) + 2 wt.% CNT	326	83

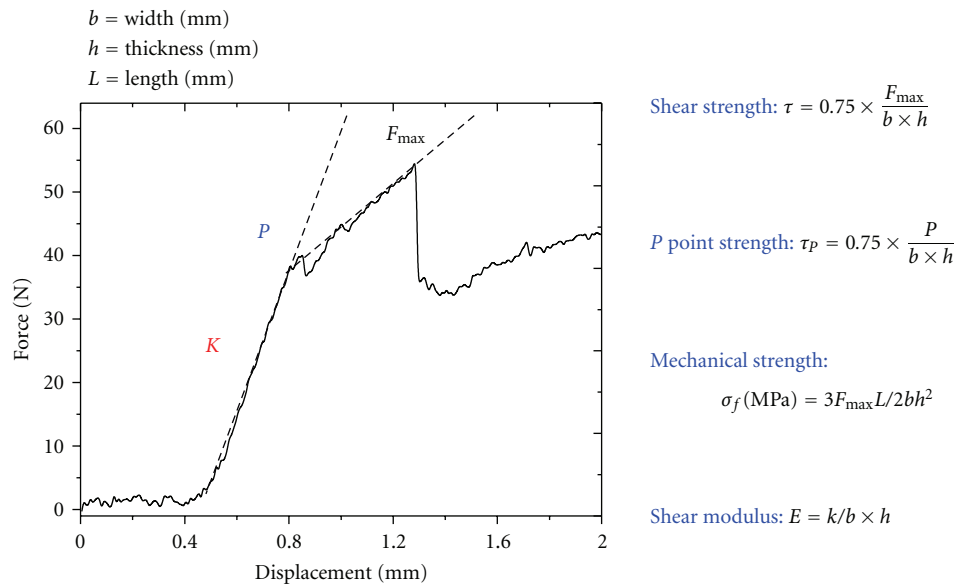


FIGURE 13: Example of a graphic of force as a function of the displacement with the mechanical properties we can deduce (right panel) from the (ASTM D2344 standard).

compare samples between them in terms of mechanical recovery.

As mentioned above, seven sets of CFRP samples specimens (12 cm \times 12 cm) were prepared for the present study. Table 3 summarizes the specification of each sample specimen.

Three kinds of self healing materials were employed:

- (i) one based on encapsulated 5E2N monomer,
- (ii) the second based on the encapsulated DCPD monomer,
- (iii) a third class based on a 50/50 wt. % mixture of these two monomers.

All the self healing materials are blended with a 1 wt. % of ruthenium Grubbs catalyst (RGC) and 10 wt. % of microcapsules.

The third class of the self-healing material was then mixed with different concentrations of SWNTs. The epoxy matrix is kept the same for all samples (namely, Epon 828 with the epicure 3046).

Figure 13 shows a typical example of a graphic of the force as a function of the displacement with the mechanical properties we can deduce from the (ASTM D2344 standard). Figure 14(a) summarizes the mechanical strengths obtained from the flexural tests performed on the CFRP samples containing different healing agents and various SWNT concentrations. The main goal is to extract the mechanical contribution of the healing part and that due to the CNT materials.

5.3. Extraction of the Self-Repair Component. When comparing to the pristine samples (i.e., containing only epoxy material), we can extract the recovery due exclusively to the

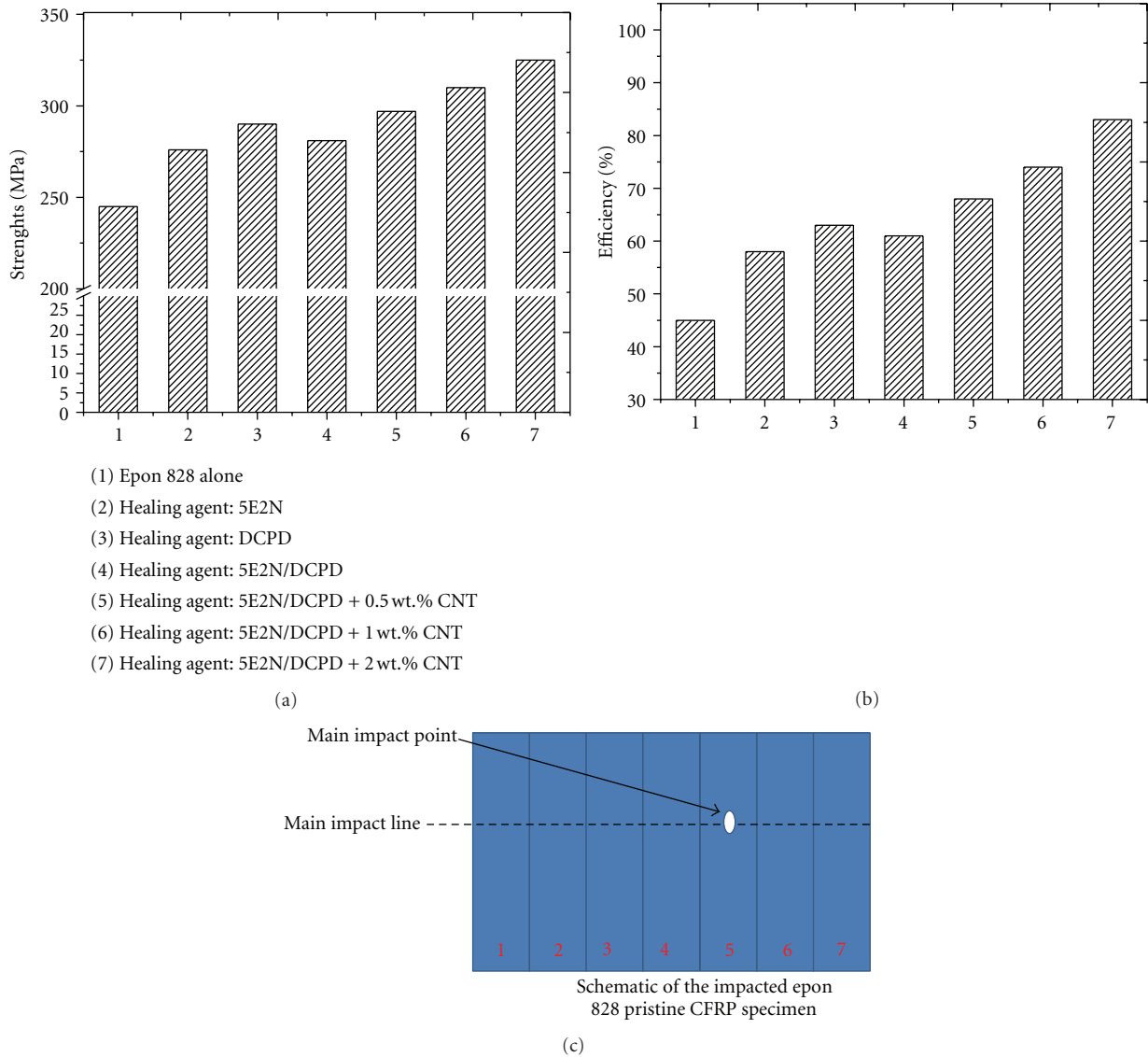


FIGURE 14: (a) Comparison of the deduced mechanical strengths, as indicator of the self healing efficiency and the CNT effect. (b) The corresponding healing efficiencies and (c) a schematic of the CFRP sample cut into different slices for the three-point bending flexural tests.

healing materials [43–46]. In doing so, we conclude the following.

- (i) 31 MPa are due exclusively to the self healing material based 5E2N, which represents an enhancement in terms of the mechanical strength of about 13%.
- (ii) When using the DCPD based healing agent, a better healing is obtained (improvement up to 18% of the mechanical strength).
- (iii) When using a mixture of 50/50 wt. % of DCPD/5E2N healing agent, a slight decrease occurred (from 18 to ~15%) in terms of the flexural strength, which is due to the incorporation of the 5E2N part (recall that the 5E2N is a linear polymer having lower mechanical strength, its addition to the DCPD slightly decreases

somehow the overall mechanical strength of the mixture.)

- (iv) A clear improvement is obtained when integrating the SWNT material, even with a concentration as low as 0.5 wt. %.
- (v) Then, an enhancement up to 81 MPa in terms of the mechanical recovery is due to the healing materials containing 2 wt. % of SWNT (comparison of the specimen #7 and #1), which represents an improvement in the mechanical strength of about 33%.

Finally, Figure 14(b) shows the comparison between the healing efficiencies (estimated as a ratio of the flexural strength obtained from the first and the second bending tests after the healing process). One can note that a healing

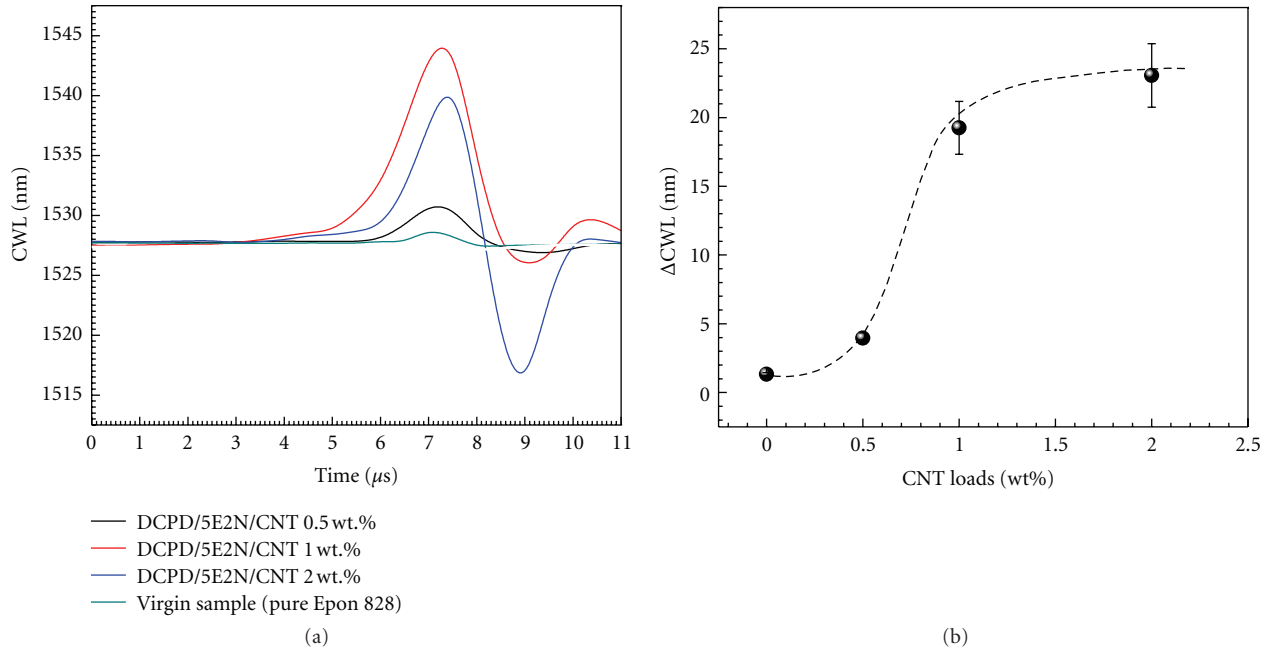


FIGURE 15: (a) FBG-center wavelength (CWL) signals with respect to the time of the impacted CFRP structures having different CNTs loads. (b) FBG-center wavelength position as a function of the CNT loads.

efficiency due to the incorporation of only 2 wt. % of SWNTs can reach the excellent value of 83%.

It is worth to mention at this level that the carbon nanotubes present in the crater zone area are supposed to disappear with the ejected mass (*ejecta*). However, those present in the delaminations zones play a crucial role in the reconstruction of the material and help the self-healed composite to repair by acting as a cross-links in the released 5E2N, polymer after its ROMP polymerization with the Grubbs catalyst.

6. Outlooks

Two main issues are presently in progress:

6.1. Damping Effects of CNT. Figure 15 shows the measured FBG-center wavelength (CWLs) signals as a function of the time. CWL were obtained for the impacted CFRP structures having a 50/50 wt. % of 5E2N/DCPD healing agent and different concentrations of CNTs. Figure 15(b) shows the extraction of FBG-center wavelength position as a function of the CNT loads.

We noted that samples with 1% and 2% CNT showed high damping effects due to the presence of a higher load of CNT. Work is actually under progress to correlate the mechanical contribution of the CNT materials to their morphological and structural properties.

6.2. FBG Monitoring the Hypervelocity Impact at 2 MHz Frequency Acquisition System. The first effects of the pellet hitting the CFRP material structures occur in the few first μs

as shown in Figure 16, where the first response can be resumed in the first 20–50 μs . After almost 1.5 ms, the direct impact effect is ended although different modes of responses can be developed by the material responding to the shock event (i.e., impact). To note that each FBG has its own signal signature, the latter depends on the FBG distance to the impact crater.

Experimental Parameters.

Bore pellet: 3 mm diameter,

Hypervelocity: 4.3 km/s,

Acquisition frequency: 2 MHz,

7. Conclusions

We successfully synthesized self-healing materials to be used mainly in space environment. The autorepair composite was blends of microcapsules containing various combinations of a 5-ethylidene-2-norbornene (5E2N) and dicyclopentadiene (DCPD) monomers, reacted with ruthenium Grubbs' catalyst (RGC). Both monomers were encapsulated into a (polyMelamine-urea-formaldehyde) (PMUF) shell material, where the capsules average size was less than 15 microns. Then, the self healing materials were mixed with a resin epoxy based Epon 828 and single-walled carbon nanotubes (SWNTs) by means of a vacuum centrifuging technique. The obtained nanocomposites were infused into the layers of woven carbon fibers reinforced polymer (CFRP). The CFRP specimens were then subjected to hypervelocity impact conditions—prevailing in the space environment—using a

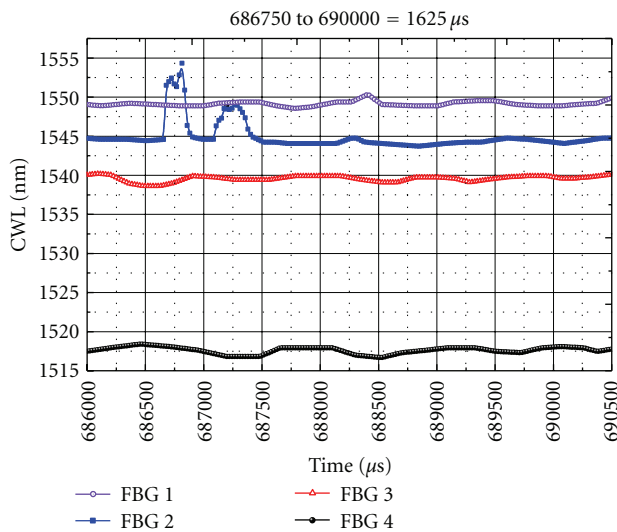


FIGURE 16: Temporal response of the FBG sensors to the pellet at hypervelocity of 4.3 km/s and a frequency acquisition of 2 MHz.

home-made implosion-driven-hypervelocity launcher. After the hypervelocity event, the three-point bending tests show clearly that the optimum self healing material having the best mechanical strength was an equal-weight blend of 5E2N and DCPD monomers, while a huge improvement in terms of the autorepair efficiency was obtained when adding small quantities of SWNT (of 2 wt. % and less). These results establish well that 5E2N/DCPD/CNT/RGC system is a realistic possibility which possess tremendous potential for space applications. However, additional experimental investigation, especially a systematic cryomicrotome analysis as a function of the carbon nanotube loads, is needed to demonstrate clearly the damping effect of the SWNT material and their role as a cross-links in the formed polymer.

Acknowledgments

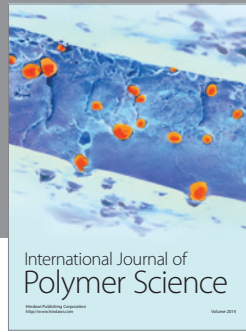
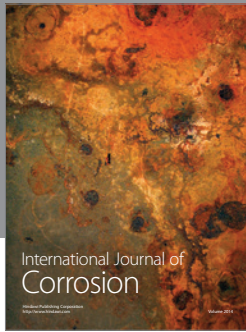
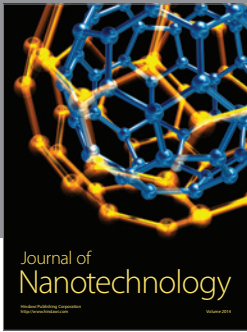
The authors would like to acknowledge the financial assistance of the Canadian Space Agency for this work. They are also grateful to Dr. Stéphane Gendron and Dr. Darius Nikanpour (CSA) for their constructive advice and support during this work.

References

- [1] R. J. Varley and S. van der Zwaag, "Towards an understanding of thermally activated self-healing of an ionomer system during ballistic penetration," *Acta Materialia*, vol. 56, no. 19, pp. 5737–5750, 2008.
- [2] S. Van der Zwaag, *Self-Healing Materials: An Alternative Approach to 20 Centuries of Materials Science*, Springer, Dordrecht, The Netherlands, 2007.
- [3] H. H. Kausch, "The nature of defects and their role in large deformation and fracture of engineering thermoplastics," *Pure and Applied Chemistry*, vol. 55, no. 5, pp. 833–844, 1983.
- [4] R. P. Sijbesma, F. H. Beijer, L. Brunsveld et al., "Reversible polymers formed from self-complementary monomers using

- quadruple hydrogen bonding," *Science*, vol. 278, no. 5343, pp. 1601–1604, 1997.
- [5] D. A. Davis, A. Hamilton, J. Yang et al., "Force-induced activation of covalent bonds in mechanoresponsive polymeric materials," *Nature*, vol. 459, no. 7243, pp. 68–72, 2009.
- [6] G. V. Kolmakov, K. Matyjaszewski, and A. C. Balazs, "Harnessing labile bonds between nanogel particles to create self-healing materials," *ACS Nano*, vol. 3, no. 4, pp. 885–892, 2009.
- [7] S. Ludingab and A. S. J. Suiker, "Self-healing of damaged particulate materials through sintering," *Philosophical Magazine*, vol. 88, no. 28–29, pp. 3445–3457, 2008.
- [8] M. Zako and N. Takano, "Intelligent material systems using epoxy particles to repair microcracks and delamination damage in GFRP," *Journal of Intelligent Material Systems and Structures*, vol. 10, no. 10, pp. 836–841, 1999.
- [9] S. M. Bleay, C. B. Loader, V. J. Hawyys, L. Humberstone, and P. T. Curtis, "A smart repair system for polymer matrix composites," *Composites A*, vol. 32, no. 12, pp. 1767–1776, 2001.
- [10] S. R. White, N. R. Sottos, P. H. Geubelle et al., "Autonomic healing of polymer composites," *Nature*, vol. 409, pp. 794–797, 2001.
- [11] D. G. Shchukin and H. Möhwald, "Self-repairing coatings containing active nanoreservoirs," *Small*, vol. 3, no. 6, pp. 926–943, 2007.
- [12] K. S. Toohey, N. R. Sottos, J. A. Lewis, J. S. Moore, and S. R. White, "Self-healing materials with microvascular networks," *Nature Materials*, vol. 6, no. 8, pp. 581–585, 2007.
- [13] T. Yin, L. Zhou, M. Z. Rong, and M. Q. Zhang, "Self-healing woven glass fabric/epoxy composites with the healant consisting of micro-encapsulated epoxy and latent curing agent," *Smart Materials and Structures*, vol. 17, no. 1, Article ID 015019, 2008.
- [14] S. H. Cho, S. R. White, and P. V. Braun, "Self-healing polymer coatings," *Advanced Materials*, vol. 21, no. 6, pp. 645–649, 2009.
- [15] J. Suhr, N. Koratkar, P. Koblinski, and P. Ajayan, "Viscoelasticity in carbon nanotube composites," *Nature Materials*, vol. 4, no. 2, pp. 134–137, 2005.
- [16] X. Sheng, M. R. Kessler, and J. K. Lee, "The influence of cross-linking agents on ring-opening metathesis polymerized thermosets," *Journal of Thermal Analysis and Calorimetry*, vol. 89, no. 2, pp. 459–464, 2007.
- [17] F. H. Gojny, M. H. G. Wichmann, U. Kopke, B. Fiedler, and K. Schulte, "Carbon nanotube-reinforced epoxy-composites: enhanced stiffness and fracture toughness at low nanotube content," *Composites Science and Technology*, vol. 64, no. 15, pp. 2363–2371, 2004.
- [18] C. Liu, Y. Y. Fan, M. Liu, H. T. Cong, H. M. Cheng, and M. S. Dresselhaus, "Hydrogen storage in single-walled carbon nanotubes at room temperature," *Science*, vol. 286, no. 5442, pp. 1127–1129, 1999.
- [19] H. Gao, Y. Kong, D. Cui, and C. S. Ozkan, "Spontaneous insertion of DNA oligonucleotides into carbon nanotubes," *Nano Letters*, vol. 3, no. 4, pp. 471–473, 2003.
- [20] L. Gao, T. W. Chou, E. T. Thostenson, Z. Zhang, and M. Coulaud, "In situ sensing of impact damage in epoxy/glass fiber composites using percolating carbon nanotube networks," *Carbon*, vol. 49, no. 10, pp. 3382–3385, 2011.
- [21] R. de Oliveira, C. A. Ramos, and A. T. Marques, "Health monitoring of composite structures by embedded FBG and interferometric Fabry-Pérot sensors," *Computers and Structures*, vol. 86, no. 3–5, pp. 340–346, 2008.

- [22] A. W. Morey, G. Meltz, and W. Glenn, "Fiber Bragg grating sensor," in *7th Fiber Optics & Laser Sensors*, vol. 1169 of *Proceedings of SPIE*, pp. 98–107, 1989.
- [23] E. Kirkby, R. de Oliveira, V. Michaud, and J. A. Manson, "Impact localisation with FBG for a self-healing carbon fibre composite structure," *Composite Structures*, vol. 94, no. 1, pp. 8–14, 2011.
- [24] A. Panopoulou, T. Loutas, D. Roulias, S. Fransen, and V. Kostopoulos, "Dynamic fiber Bragg gratings based health monitoring system of composite aerospace structures," *Acta Astronautica*, vol. 69, no. 7-8, pp. 445–457, 2011.
- [25] G. A. Graham and A. T. Kearsley, "Study of smaller impact craters on HST solar cells," Final Report contract no. 13308/98/NL/MV, Oxford Brookes University-ESA-ESTEC, 1999.
- [26] L. J. Nicholas, "Preserving the near-earth space environment with green engineering and operations," NASA Green Engineering Masters Forum, NASA Johnson Space Center, 2009.
- [27] IADC Protection Manual, <http://www.iadc-online.org>.
- [28] O. Smiljanic, B. L. Stansfield, J. P. Dodelet, A. Serventi, and S. Désilets, "Gas-phase synthesis of SWNT by an atmospheric pressure plasma jet," *Chemical Physics Letters*, vol. 356, no. 3-4, pp. 189–193, 2002.
- [29] O. Smiljanic, F. Larouche, X. Sun, J. P. Dodelet, and B. L. Stansfield, "Synthesis of single-walled carbon nanotubes (C-SWNTs) with a plasma torch: a parametric study," *Journal of Nanoscience and Nanotechnology*, vol. 4, no. 8, pp. 1005–1013, 2004.
- [30] S. Bandow, S. Asaka, Y. Saito et al., "Effect of the growth temperature on the diameter distribution and chirality of single-wall carbon nanotubes," *Physical Review Letters*, vol. 80, no. 17, pp. 3779–3782, 1998.
- [31] X. Liu, X. Sheng, J. Lee, and M. R. Kessler, "Synthesis and characterization of melamine-urea-formaldehyde microcapsules containing ENB-based self-healing agents," *Macromolecular Materials and Engineering*, vol. 294, no. 6-7, pp. 389–395, 2009.
- [32] B. Aïssa, E. Haddad, W. Jamroz et al., "Micromechanical characterization of single-walled carbon nanotube reinforced ethylidene norbornene nanocomposites for self-healing applications," *Smart Materials and Structures*, vol. 21, no. 10, Article ID 105028, 2012.
- [33] B. Aïssa, R. Nechache, E. Haddad, W. Jamroz, P. E. Merle, and F. Rosei, "Ruthenium Grubbs' catalyst nanostructures grown by UV-excimer-laser ablation for self-healing applications," *Applied Surface Science*, vol. 258, no. 24, pp. 9800–9804, 2012.
- [34] S. Varghese, A. Lele, and R. Mashelkar, "Metal-ion-mediated healing of gels," *Journal of Polymer Science A*, vol. 44, no. 1, pp. 666–670, 2006.
- [35] J. M. Asua, "Miniemulsion polymerization," *Progress in Polymer Science*, vol. 27, no. 7, pp. 1283–1346, 2002.
- [36] B. J. Blaiszik, M. M. Caruso, D. A. McIlroy, J. S. Moore, S. R. White, and N. R. Sottos, "Microcapsules filled with reactive solutions for self-healing materials," *Polymer*, vol. 50, no. 4, pp. 990–997, 2009.
- [37] E. B. Murphy and F. Wudl, "The world of smart healable materials," *Progress in Polymer Science*, vol. 35, no. 1-2, pp. 223–251, 2010.
- [38] E. N. Brown, M. R. Kessler, N. R. Sottos, and S. R. White, "In situ poly(urea-formaldehyde) microencapsulation of dicyclopentadiene," *Journal of Microencapsulation*, vol. 20, no. 6, pp. 719–730, 2003.
- [39] A. J. Patel, S. R. White, D. M. Baechle, and E. D. Wetzel, "Self-healing composite armor-self-healing composites for mitigation of impact damage in U.S. Army applications," Final Report contract no. W9 11 NF-06-2-0003, U.S. Army Research Laboratory, 2006.
- [40] E. N. Brown, S. R. White, and N. R. Sottos, "Microcapsule induced toughening in a self-healing polymer composite," *Journal of Materials Science*, vol. 39, no. 5, pp. 1703–1710, 2004.
- [41] B. J. Blaiszik, N. R. Sottos, and S. R. White, "Nanocapsules for self-healing materials," *Composites Science and Technology*, vol. 68, no. 3-4, pp. 978–986, 2008.
- [42] K. S. Suslick and G. Price, "Applications of ultrasound to materials chemistry," *Annual Review of Materials Research*, vol. 29, pp. 295–326, 1999.
- [43] X. Liu, X. Sheng, J. K. Lee, and M. R. Kessler, "Isothermal cure characterization of dicyclopentadiene The glass transition temperature and conversion," *Journal of Thermal Analysis and Calorimetry*, vol. 89, no. 2, pp. 453–457, 2007.
- [44] X. Liu, X. Sheng, J. K. Lee, M. R. Kessler, and J. S. Kim, "Rheokinetic evaluation of self-healing agents polymerized by Grubbs catalyst embedded in various thermosetting systems," *Composites Science and Technology*, vol. 69, no. 13, pp. 2102–2107, 2009.
- [45] E. T. Thostenson and T. W. Chou, "Processing-structure-multi-functional property relationship in carbon nanotube/epoxy composites," *Carbon*, vol. 44, no. 14, pp. 3022–3029, 2006.
- [46] W. P. Schonberg and F. Yang, "Response of space structures to orbital debris particle impact," *International Journal of Impact Engineering*, vol. 14, no. 1-4, pp. 647–658, 1993.



Hindawi

Submit your manuscripts at
<http://www.hindawi.com>

